DOI: 10.1111/cgf.14653
Pacific Graphics 2022
N. Umetani, E. Vouga, and C. Wojtan
(Guest Editors)

Volume 41 (2022), Number 7

Point-augmented bi-cubic subdivision surfaces

K. Karčiauskas[1] and J. Peters[2]

[1]Vilnius University
[2] University of Florida

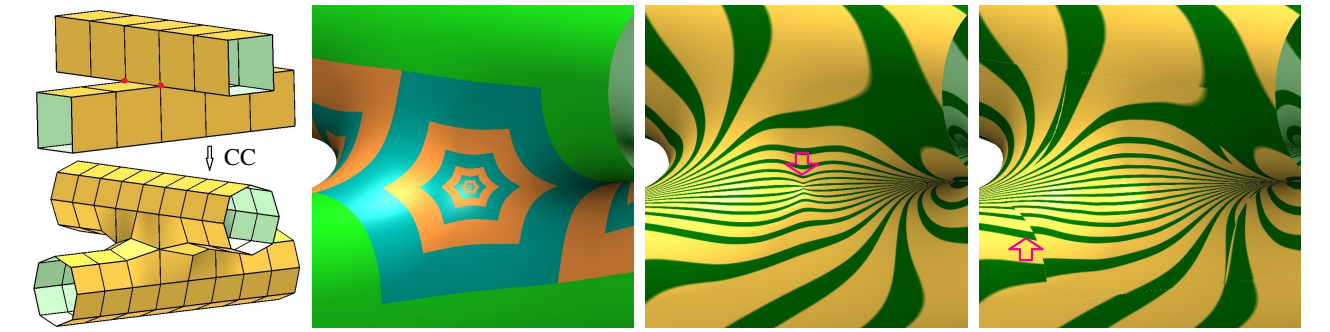

(a) mesh (b) layout of surface rings (c) Catmull-Clark (CC) (d) Ma-Ma (MM)

(e) CC-transition + MM (f) new PAS2: 2×2 bi-3 (g) mean curvature of (f) (h) new PAS1: C^1 bi-3

Figure 1: *Comparison of bi-cubic (bi-3) subdivision algorithms. (a) Input: once Catmull-Clark refined beams. (b) Contracting rings of 6-sided bi-cubic (bi-3) subdivision pieces surrounded by regular bi-3 splines. (c–f,h) highlight lines [BC94] (points to flaws) of (c) Catmull-Clark (CC) [CC78], (d) Ma-Ma (MM) [MM18], (e) 1 CC step followed by MM, (f) new Point-augmented 2×2 bi-3 Subdivision (PAS2), (g) mean curvature of PAS2, (h) new Point-augmented C^1 bi-3 Subdivision (PAS1).*

Abstract

Point-Augmented Subdivision (PAS) replaces complex geometry-dependent guided subdivision, known to yield high-quality surfaces, by explicit subdivision formulas that yield similarly-good limit surfaces and are easy to implement using any subdivision infrastructure: map the control net $\mathbf{d}$ *augmented by a fixed central limit point* $\mathbf{C}$*, to a finer net* $(\breve{\mathbf{d}}, \mathbf{C}) = M(\mathbf{d}, \mathbf{C})$*, where the subdivision matrix* M *is assembled from the provided stencil Tables. Point-augmented bi-cubic subdivision improves the state of the art so that bi-cubic subdivision surfaces can be used in high-end geometric design: the highlight line distribution for challenging configurations lacks the shape artifacts usually associated with explicit iterative generalized subdivision operators near extraordinary points. Five explicit formulas define Point-augmented bi-cubic subdivision in addition to uniform B-spline knot insertion. Point-augmented bi-cubic subdivision comes in two flavors, either generating a sequence of* C^2*-joined surface rings (PAS2) or* C^1*-joined rings (PAS1) that have fewer pieces.*

1. Introduction

Subdivision Surfaces are widely used in computer graphics [DKT98] but less so for geometric design [Ma05], due to shape artifacts [SB03, KPR04], see also Fig. 1c,d,e. While subdivision rules map a net of control points to a refined net [DS78], subdivision surfaces are best viewed as a sequence of smoothly-joined contracting surface rings [PR08], see Fig. 1b. For Catmull-Clark (CC) subdivision [CC78], each of the n sectors of a surface ring consists of three bi-3 patches. For Ma-Ma (MM) subdivision [MM18] and similar curvature bounded variants, see Fig. 2, they consist of three 2×2 macro-patches, i.e. 12 bi-3 patches per sector, to accommodate the more complicated refinement rules. Our new Point-augmented bi-cubic subdivision (PAS) has two corresponding flavors that differ only in the surface generating systems associated with the points of the control net.

The new Point-augmented bi-cubic subdivision (PAS) algorithm delivers a sequence of bi-cubic (bi-3) surface rings that promote subdivision as a tool for higher-end design. PAS has the following new features.

- The central limit point **C**, marked as • in Fig. 3 is fixed at the outset.
- The refinement rules for the $6n$ innermost new control nodes • depend on all $12n$ input nodes and the central point **C**. (New control nodes marked ∘ are defined by uniform B-spline knot insertion, a.k.a. regular rules).
- Due to symmetry of construction, we need only specify five special refinement rules and these have explicit formulas (listed in the Appendix for $n = 3,5,6,7,8,9$).
- The surface rings of PAS2 join C^2, the surface rings of PAS1 join C^1. In either case, the limit surface is C^1 at **C**.
- Good highlight line distributions of PAS surfaces on a series of challenging input nets demonstrate suitability of PAS for higher-end design (see Section 6).

Fig. 1 illustrates the advance due to PAS over the state-of-the-art. The top quadrilateral mesh in Fig. 1a consists of the two beams with irregular nodes of valence 6, marked as •. One CC refinement step separates the irregular nodes. Continued Catmull-Clark refinement results in pinched highlight lines near the limit point, see Fig. 1c. Ma-Ma (MM) subdivision [MM18] removes the pinching, but does not even join C^0 with the surrounding surface and neighboring subdivision regions, see Fig. 1d; and requires an additional CC step, see Fig. 1e. Point-augmented 2×2 bi-3 Subdivision (PAS2), see Fig. 1f, removes oscillations visible in Fig. 1e, both in the transition and moving towards the irregular center. Although formally only C^1 at the limit point, the mean curvature appears continuous and even smooth in Fig. 1g. The sibling of PAS2, Point-augmented C^1 bi-3 Subdivision (PAS1), consists of C^1-joined rings. Visually, without extreme zoom, PAS1 surfaces look like PAS2 surfaces, see Fig. 1h, and have similar curvature distributions.

Overview Section 2 reviews the literature and basics of subdivision surfaces with focus on bi-cubic subdivision. Section 3 presents the PAS algorithms whose explicit refinement formulas are listed in the Appendix. Section 4 analyses the limit surfaces near the extraordinary point. For the reader interested in the derivation, Section 5 explains the underlying approach and techniques. A reader primarily interested in applying PAS to generate well-shaped surfaces can skip Section 5. Section 6 compares the surfaces generated by PAS to [CC78, MM18, MM19] and two guided curvature bounded subdivision algorithms [KP19].

2. Bi-cubic subdivision: structure and literature

The input control net to Catmull-Clark (CC) subdivision is the **c**-net formed by the nodes marked as • in Fig. 2a, *left*. Adding one layer of quadrilateral facets yields an extended **c**-net. This extended **c**-net defines one surrounding regular bi-cubic ring, see Fig. 2b, *left*, to judge the transition to a regular bi-3 spline. An extended **c**-net is also required as input control net for conventional curvature-bounded algorithms, such as [Sab91] and Ma-Ma (MM) subdivision. Unlike guided or the new PAS subdivision, conventional curvature-bounded algorithms do not preserve the regular bi-3 ring and this causes the differentiability problems demonstrated in Fig. 1d. Therefore, that class of algorithms requires an initial Catmull-Clark refinement step as in Fig. 1e and explained in Section 6.

For CC subdivision (Fig. 2a, *middle*) all but the central refined nodes are defined by B-spline knot insertion [dB78]. The refined nodes define a smaller bi-3 ring, and the sequence of rings join C^2 as they contract towards the limit point **C**, see Fig. 2b, *right*. The highlight lines join smoothly at the transition, but the simple rules cause undesirable pinching of highlight lines near **C**.

Bi-cubic curvature-bounded subdivision variants consider special valence-dependent rules also for the $2n$ nearest neighbors of irregular node [Sab91]. The generating system produces a per step three 2×2 macro-patches in each of the n sectors. Convex faceted quad nets result in undue flatness near **C** or oscillate due to their operator's eigenstructure. Of the classic curvature-bounded variants of CC subdivision, Ma-Ma subdivision [MM18] applies the most extensive tuning [ADS11] and, arguably, most improves the shape. [MM19] achieves uniform contraction due to a subdominant eigenvalue $\lambda = 1/2$ but reveals more pronounced ripples. The shape and even curvature and highlight line distribution of the 3×3 and 2×2 macro-patch constructions of [KP19] are very similar to *PAS*2. However [KP19] requires the separate generation of a guide surface, while PAS2 requires exclusively uniform application of subdivision rules. The elimination of the initial guide construction from the subdivision algorithm is a major contribution of the new algorithm.

The bi-3 surface construction [KP22] only applies to very special, though often occurring MSV control nets where all irregular nodes have the same valence. When the mesh is MSV then [KP22] is more efficient than PAS and the quality is alike (compare Fig.16 of [KP22] to Fig. 15b). The completion surfaces in [KP21] are of degree bi-4 and the construction is heterogeneous.

For AS, we focus on a **d**-net, see Fig. 3a. While we can derive a **d**-net from a **c**-net, the algorithm assumes as input a **d**-net (without extraordinary node) and a fixed central point **C** since all our systematic attempts to obtain rules with good shape properties directly from the **c**-net failed. Note that by adding **C** to the **d**-net the augmented net resembles a **c**-net; however **C** is a fixed point, not a mesh node. Fig. 3b displays nodes that define a C^2 bi-3 surface ring, analogous to Fig. 2b, but here using 2×2 macro-patches as for MM

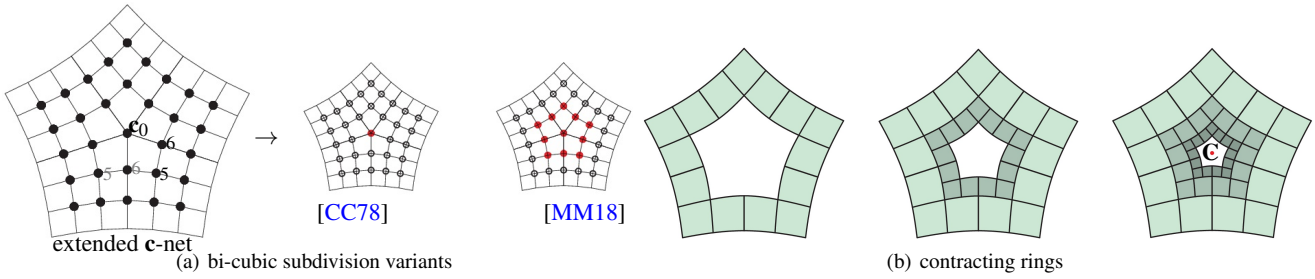

(a) bi-cubic subdivision variants (b) contracting rings

Figure 2: *Bi-3 subdivision pattern. (a) original Catmull-Clark and curvature-bounded schemes; (b) contracting rings and a limit point* **C** ●.

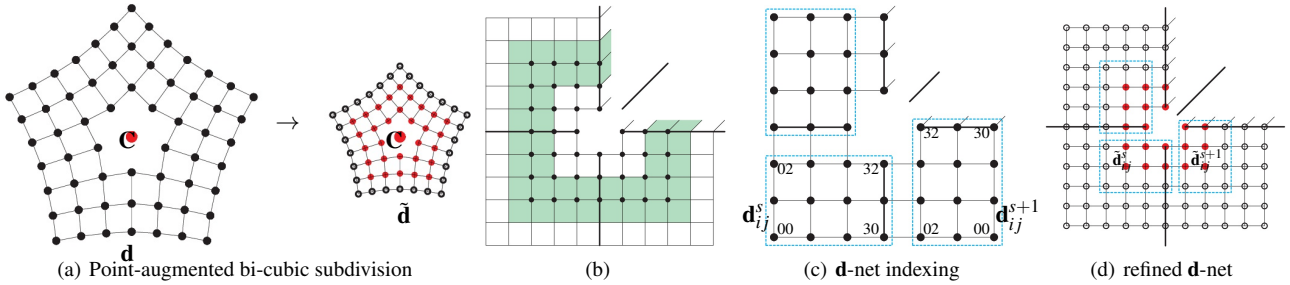

(a) Point-augmented bi-cubic subdivision (b) (c) **d**-net indexing (d) refined **d**-net

Figure 3: *Point-augmented bi-cubic subdivision of the control* **d***-net to* $\tilde{\mathbf{d}}$ *(a). (b)* C^2 *bi-3 B-spline control points defining one ring of* $3n$ 2×2 *macro-patches. (c) Indexing of the* **d***-net sectors and (d) its refinement:* ○ *regular refinement,* ● *new rules.*

subdivision. The nodes, marked as • in Fig. 3a,b form the **d**-net and define a second-order Hermite prolongation from the surrounding surface. Fig. 3c shows the indexing and grouping into cyan-boxed sectors and Fig. 3a, *right* and Fig. 3d show the refined **d**-net. The refined control points marked ○ are defined by uniform knot insertion, a.k.a. regular (bi-cubic subdivision) rules. The refined control points marked • require, due to rotational symmetry, just six new (PAS) subdivision rules (five due to flip symmetry across the sector diagonals). Together the new points define a new bi-3 ring of 2×2 macro-patches that joins C^2 to its predecessor. The challenge is to obtain surface shape that is superior to that generated by earlier bi-3 subdivision algorithms.

The central idea of PAS is to replicate the good surface quality of guided subdivision by including in each step, without explicit computation, a piecewise polynomial guide. Unlike guided subdivision, where the guide is explicitly computed and fixed at the outset, in PAS, the guide is symbolically computed and integrated into the stencils and slightly changes in each refinement step. The integration of the guides yields simplicity and efficiency while the guide sequence provides good quality. Different flavors of this idea have appeared before, see e.g. [Pra97, Lev06, KP07]. In fact, the new PAS algorithms are closely related to guided subdivision algorithms [KP18] but avoid their procedural and non-explicit double construction. Guided subdivision first constructs a guide surface (that approximates the surrounding data and focusses on the central shape) and second, iteratively samples the guide so the subdivision surface rings follow the guide shape. Due to the static limit shape, guided subdivision can generate surfaces with good highlight line distributions for a wide variety of guide constructions.

PAS takes advantage of the robustness of the guided approach. However, applying PAS requires neither the construction of a guide surface nor its sampling: the subdivision rules have explicit formulas (stencils) as do CC and MM, for example. While PAS can be viewed as having a built-in guide (see Section 5), this guide is carefully selected to avoid artifacts arising from iterative application of subdivision operators (matrix multiplication) that can unduly favor eigenfunctions and so lead to oscillations.

If the input net is a **c**-net, applying uniform bi-3 spline subdivision rules to the **c**-net yields a **d**-net and we choose **C** to be the extraordinary limit point of Catmull-Clark subdivision [HKD93], slightly adjusted for $n=3$. With $\mathbf{c}_0$ the central node, $\mathbf{c}_6^s$ its direct neighbor node in sector $s\in\{0,\dots,n-1\}$ and $\mathbf{c}_5^s$ its diagonal neighbor, see Fig. 2a:

$$\mathbf{C} := \begin{cases} \frac{n}{n+5}\mathbf{c}_0 + \frac{4}{n(n+5)}\sum_{s=0}^{n-1}\mathbf{c}_6^s + \frac{1}{n(n+5)}\sum_{s=0}^{n-1}\mathbf{c}_5^s, & n>4,\\ \frac{11}{32}\mathbf{c}_0 + \frac{1}{6}\sum_{s=0}^{n-1}\mathbf{c}_6^s + \frac{5}{96}\sum_{s=0}^{n-1}\mathbf{c}_5^s, & n=3. \end{cases} \tag{1}$$

When the input is a **d**-net, **C** is determined by applying uniform bi-3 spline subdivision rules to the $6n+1$ nodes of an (as of yet undetermined) **c**-net and minimizing the sum of squared distances to the corresponding nodes to the given **d**-net. The resulting **c**-net defines **C** by (1). An explicit calculation using a symbolic solver, here Maple, yields the explicit solution for **C** in terms of the **d**-net:

$$\mathbf{C} := \sum_{s=0}^{n-1}\sum_{i=0}^{3}\sum_{j=0}^{2} e_{ij}\mathbf{d}_{ij}^s\,. \tag{2}$$

$$e_{10} := -4e_{00},\ e_{11} := 16e_{00},\ e_{21} := -4e_{20},\ e_{31} := -4e_{30},$$
$$e_{01} := e_{10},\ e_{02} := e_{20},\ e_{12} := e_{21};$$

$$n>4: \gamma := 287n(n+5);$$
$$e_{00} := \frac{79n-269}{4\gamma},\ e_{20} := \frac{1985n-4899}{28\gamma},\ e_{30} := \frac{208n-592}{\gamma},$$
$$e_{22} := \frac{1247n-61}{4\gamma},\ e_{32} := \frac{5928n-5392}{7\gamma};$$

$$n=3: e_{00} := \frac{-5}{13776},\ e_{20} := \frac{55}{32144},\ e_{30} := \frac{5}{3444},$$
$$e_{22} := \frac{1723}{13776},\ e_{32} := \frac{1363}{6027}.$$

3. The subdivision algorithm: $(\mathbf{d},\mathbf{C}) \to (\tilde{\mathbf{d}},\mathbf{C})$

The six outer new nodes $\tilde{\mathbf{d}}^s_{h0}$, $h=0,1,2,3$ and $\tilde{\mathbf{d}}^s_{0k}$, $k=1,2$, (note the accent $\sim$ of the refined nodes) are defined by regular refinement rules (uniform bi-cubic B-spline knot insertion). By symmetry, we can focus on one sector $s\in\{0,\dots,n-1\}$. The six special rules for new nodes $\tilde{\mathbf{d}}^s_{hk}$, $h=1,2,3, k=1,2$, (• in Fig. 3a) have the formulas

$$\tilde{\mathbf{d}}^s_{hk} := a^{hk}_0\mathbf{C} + \sum_{r=0}^{n-1}\sum_{i=0}^{3}\sum_{j=0}^{2} a^{r,hk}_{ij}\mathbf{d}^{s+r}_{ij}, \tag{3}$$

equivalent to applying a $6\times(1+12n)$ matrix. By symmetry of the formulas, the rules for $\tilde{\mathbf{d}}^s_{12}$ mirror those of $\tilde{\mathbf{d}}^s_{21}$. By partition of unity, the weight corresponding to $\mathbf{C}$ is $a^{hk}_0 := 1-\sum_{r=0}^{n-1}\sum_{i=0}^{3}\sum_{j=0}^{2} a^{r,hk}_{ij}$. The inner double summation with indices shown in Fig. 3c is unfolded into a 4×3 vector with indices 00 10 20 30 01 11 21 31 02 12 22 32 to form the rows of each of the five matrices $A^n_{11}, A^n_{22}, A^n_{21}, A^n_{31}, A^n_{32}$ where the superscript n is the valence and the subscript is the index of the new node. These matrices define the full PAS operator and are listed in the Appendix. Each refinement step results in sufficiently many new regular uniform B-spline control points to generate a sequence of smoothly-joined bi-3 surface rings. For PAS2, see Fig. 3b and Fig. 4 each ring consists of $3n$ macro-patches of 2×2 polynomial pieces. PAS1 sub-samples this data (see Section 5.3) to generate $3n$ bi-3 pieces per step.

4. Analysis

The full Point-augmented bi-cubic subdivision matrix is of size $(12n+1)\times(12n+1)$. The equations for computing the eigenvalues of the subdivision matrix were set up directly, without discrete Fourier transform and symbolically using the software Maple and the sub-matrices of the Appendix. As expected, one eigenvalue dominates and is 1, and $\mathbf{C}$ is the corresponding extraordinary point. The double subdominant eigenvalue λ differs from that of Catmull-Clark subdivision by at most 10^{-3}, for $n\in\{3,5,6,7,8,9,10\}$. This too is expected, since the refinement rules are derived using a linear transformation of the characteristic ring of Catmull-Clark subdivision (see Section 5). With μ the subsubdominant eigenvalue, the deviation of $\frac{\mu}{\lambda^2}$ from 1, required for curvature continuity, is small:

n	3	5	6	7	8	9	10
$\frac{\mu}{\lambda^2}$	0.99861	0.999	1.00823	1.02482	1.04282	1.06817	1.07965

This is a consequence of the piecewise polynomial guide baked into the derivation of the refinement rules. Formally, for $n<6$ the surface curvature converges to zero, and for $n\geq 6$ it is unbounded.

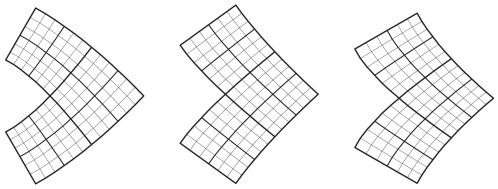

(a) $n=3$ (b) $n=5$ (c) $n=6$

Figure 4: *One sector of the characteristic ring (a.k.a characteristic map, natural configuration) of PAS2 subdivision.*

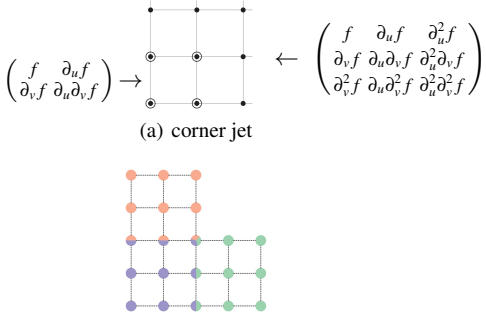

(a) corner jet

(b) bi-4 L-shape

Figure 5: *(a) Partial derivatives → BB-form. (b) Forming L-shaped tensor-border of degree bi-4.*

Practically, the ratio differs so little from 1 that curvature display of the first ten refinement steps shows neither effect. The control-net-refining subdivision rules are the same for PAS1 and PAS2, implying that the eigenstructure and limit point are the same.

We check injectivity of the characteristic ring numerically and by inspection: for $n=3,5,\dots,10$, the BB-nets of the characteristic rings are visually identical to those of Catmull-Clark subdivision, with its bi-3 patches split 2×2 for PAS2. Fig. 4 displays the characteristic rings of PAS2 for $n=3,5,6$.

5. Derivation of the refinement rules

This section is technical and intended for the specialist to trace the derivation steps; the material is not required for implementation or to otherwise reproduce PAS. After introducing the toolkit in Section 5.1, Section 5.2 lists the steps for deriving the subdivision rules. Section 5.3 derives PAS1.

5.1. Jets, tensor-borders and the bijection R

The bivariate Bernstein-Bézier form (BB-form, [dB87, Far88]) of a bivariate polynomial of degree d uses products of Bernstein polynomials $B^d_k(t) := \binom{d}{k}(1-t)^{d-k}t^k$ to define the polynomial pieces (patches)

$$\mathbf{f}(u,v) := \sum_{i=0}^{d}\sum_{j=0}^{d}\mathbf{b}_{ij}B^d_i(u)B^d_j(v), \quad 0\leq u,v\leq 1.$$

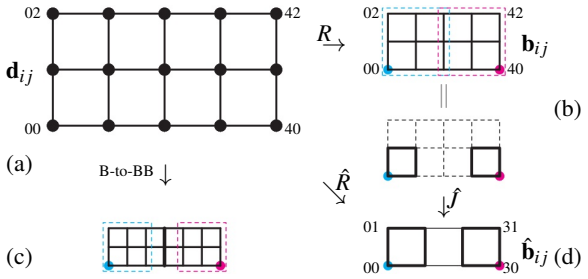

Figure 6: *(a) The subnet* $\mathbf{d}_{ij}$, $i=0,\dots,4$, $j=0,1,2$ *consists of a complete sector* $\mathbf{d}^s_{ij}$ *plus* $\mathbf{d}^{s+1}_{i2}$, $i=0,1,2$. *Degree bi-3 B-to-BB conversion generates (c) the* 3×3 *jets at the corners* • *and* •. *Alternatively, the* invertible *map R maps the subnet* $\mathbf{d}_{ij}$ *to (b) a bi-4 tensor-border* $\mathbf{b}_{ij}$, $i=0,\dots,4$, $j=0,1,2$. *(d) The map* $\hat{R}$ *is used to construct the PAS1 generating system, see Section 5.3.*

Connecting the *BB-coefficients* $\mathbf{b}_{ij}\in\mathbb{R}^3$ to $\mathbf{b}_{i+1,j}$ and $\mathbf{b}_{i,j+1}$, wherever well-defined, yields the *BB-net*. Taylor expansions at corners of patches and along boundary curves of patches are called *jet* and *tensor-border*, respectively. The second-order jet of a map f at corner point of domain square can be collected into a 3×3 BB-subnet in degree bi-d form, see Fig. 5a; and the first-order jet into a 2×2 BB-subnet marked as ○. Converting between degrees is straightforward. BB-subnets at corners of the domain square can be merged (their BB-coefficients averaged at overlapping locations), for example to form an *L-shape* of two tensor-borders of degree bi-4, see Fig. 5b.

For the derivation of the refinement rules, Fig. 6, *top*, illustrates an important bijection

$$R:\mathbf{d}_{ij}\to\mathbf{b}_{ij}$$

between a sub-net of the **d**-net and a piece of the bi-4 tensor-border. By rotational and diagonal sector symmetry, this bijection extends to the full **d**-net and all C^2-connected L-shaped bi-4 tensor-borders. R is defined as follows. The 3-fold knot insertion at the knots of a uniform bi-cubic B-spline [dB87, Far88] converts the spline to the BB-form of degree 3. This B-to-BB conversion, applied in both parameters u and v to the **d** arrangement in Fig. 6a, yields two C^2-connected bi-3 tensor-borders, see Fig. 6c. The cyan and magenta 3×3 jets at the corner points marked •, • in (b) and correspondingly in (c) represent the same Hermite data. Comparison of these jets yields the formulas of R:

$$\begin{aligned}
\mathbf{d} &:= [\mathbf{d}_{00},\mathbf{d}_{10},\mathbf{d}_{20},\mathbf{d}_{01},\mathbf{d}_{11},\mathbf{d}_{21},\mathbf{d}_{02},\mathbf{d}_{12},\mathbf{d}_{22}]^T,\\
\mathbf{b}_{00} &:= \frac{1}{36}[1,4,1,4,16,4,1,4,1]\mathbf{d},\\
\mathbf{b}_{10} &:= \frac{1}{72}[-1,8,5,-4,32,20,-1,8,5]\mathbf{d},\\
\mathbf{b}_{11} &:= \frac{1}{144}[1,-8,-5,-8,64,40,-5,40,25]\mathbf{d},\\
\mathbf{b}_{20} &:= \frac{1}{6}(\mathbf{d}_{20}+4\mathbf{d}_{21}+\mathbf{d}_{22}),\\
\mathbf{b}_{21} &:= \frac{1}{12}(-\mathbf{d}_{20}+8\mathbf{d}_{21}+5\mathbf{d}_{22}),\quad \mathbf{b}_{22}:=\mathbf{d}_{22}.
\end{aligned}\tag{4}$$

Symmetry with respect to sector diagonals and rotation defines the remaining BB-coefficients and in particular $\mathbf{b}_{01}$, $\mathbf{b}_{02}$, $\mathbf{b}_{12}$ are obtained from $\mathbf{b}_{10}$, $\mathbf{b}_{20}$, $\mathbf{b}_{21}$ by replacing $\mathbf{d}_{ij}$ by $\mathbf{d}_{ji}$; $\mathbf{b}_{3j}$, $\mathbf{b}_{4j}$, $j=0,1,2$ are obtained from $\mathbf{b}_{1j}$ and $\mathbf{b}_{0j}$ by replacing $\mathbf{d}_{ij}$ by $\mathbf{d}_{4-i,j}$.

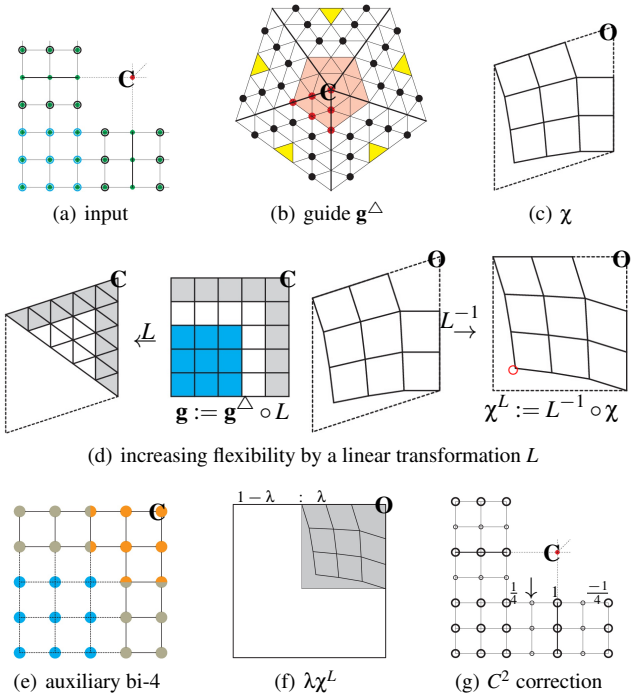

Figure 7: *Construction of guide surface* **g** *and its sampling.* **O** *denotes a common origin of sector domains;* **g** *maps* **O** *to* **C**.

5.2. Sampling guide surfaces

We now derive the subdivision rules in a sequence of steps. The symbolic formulas of a surface piece **g** are defined in terms of **C** and **d**-net and sampled to generate formulas of the refined $\tilde{\mathbf{d}}$-net in terms of **d** and **C**.

0. We apply the map R to the **d**-net to obtain n C^2-connected bi-4 L-shaped tensor-borders. Fig. 7a shows one sector and its neighboring BB-coefficients.

1. We start with a map $\mathbf{g}^{\triangle}$ of total degree 5 [Far88], see Fig. 7b. The light-red subnets share a unique quadratic expansion defined by six •. Adjacent sectors of $\mathbf{g}^{\triangle}$ join C^1, regardless of the choice of the $6n$ BB-coefficients marked •. The $3n$ yellow-underlaid coefficients do not affect C^1-join between sectors and are not used in the construction.

2. Denote as χ the tensor-border of the characteristic ring of Catmull-Clark subdivision, see Fig. 7c. Then $\mathbf{g}^{\triangle}\circ\chi$ is sampled to yield bi-4 tensor-borders **t**. The coefficients • of $\mathbf{g}^{\triangle}$ are set so that the $6n$ BB-coefficients of **t** marked as tiny ○ in Fig. 7g agree with the $6n$ BB-coefficients of the input tensor-border, marked ○ (with green interior) in Fig. 7a. This requires symbolically solving n linear systems of size 6×6, not one system of size $6n\times 6n$.

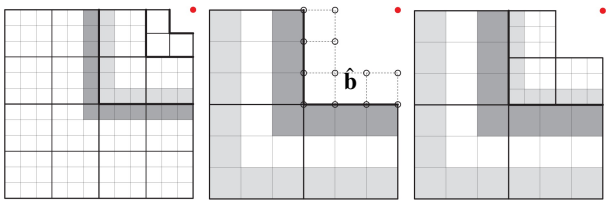

(a) bi-3 rings (b) C^1 extension (c) split of new ring

Figure 8: *Change of generating system: from* 2×2 *bi-3 macro-patches to single bi-3 patches.* • *represents* $\mathbf{C}$.

3. Composing a linear shear map L (that transforms a unit square into unit-edge parallelogram with opening angle $\frac{2\pi}{n}$, see Fig. 7d, *left*) with each sector of $\mathbf{g}^{\triangle}$ yields the structure of $\mathbf{g}$ as n bi-5 patches. The patches join G^1 due to the gray-underlaid BB-subnets; the remaining BB-coefficients do not affect G^1-continuity and are free to increase the flexibility of $\mathbf{g}$ over $\mathbf{g}^{\triangle}$.

4. Sampling the 3×3 corner jets of $\mathbf{g}\circ\chi^L$ in bi-4 form where $\chi^L := L^{-1}\circ\chi$ and joining the jets by averaging the coefficients at overlapping locations, yields an auxiliary map $\bar{\mathbf{g}}$, see Fig. 7e. The 3×3 BB-coefficients of $\bar{\mathbf{g}}$, marked as •, are still free to be set. They are set so that the 3×3 corner jet of $\bar{\mathbf{g}}\circ\chi^L$, sampled in bi-4 form at ○ in Fig. 7d, *right*, matches the input tensor-border jet marked ○ (with green interior) in Fig. 7a. Then the 4×4 BB-coefficients of $\mathbf{g}$ underlaid cyan in Fig. 7d are set to those of $\bar{\mathbf{g}}$, degree-raised to bi-5 form.

5. All BB-coefficients of $\mathbf{g}$ are now affine combinations of the $\mathbf{d}$-net and six BB-coefficients • in Fig. 7b. We choose the central • as $\mathbf{C}$ and the remaining five • to minimize the functional $\mathcal{F}_4 g := \int_0^1\int_0^1 \sum_{i+j=4,i,j\geq 0} \frac{4!}{i!j!}(\partial_s^i\partial_t^j g(s,t))^2\, ds\, dt$ over all n bi-5 sectors of $\mathbf{g}$. This functional is a heuristic, tested superior over a number of alternative formulations.

6. The refinement step, see Fig. 7f. Let λ be a subdominant eigenvalue of Catmull-Clark subdivision. The domain square of each bi-5 sector of $\mathbf{g}$ is scaled by λ towards $\mathbf{O}$ to become the gray subdomain; χ^L is also scaled by λ. (This choice is most compatible with uniform splines; other λ can be chosen but retaining good shape then requires additional work.) Sampling the scaled subdomain with the scaled χ^L yields the L-shaped bi-4 tensor-borders displayed in Fig. 7g. Since the adjacent L-shaped pieces are only C^1-connected, the columns of BB-coefficients ○ marked by ↓ are modified by the displayed stencil to have sectors join C^2.

7. Applying R^{-1} to the C^2-joined L-shapes of Fig. 7g yields the refined nodes $\tilde{\mathbf{d}}^s_{ij}$, $i=1,\ldots,3$, $j=1,2$, $s=0,\ldots,n-1$. (We recall that the remaining nodes are obtained via regular refinement.)

5.3. PAS1: derivation of C^1 bi-3 subdivision surfaces

Since the control-net-refining subdivision rules of PAS1 and PAS2 are the same, the eigenstructure and limit point are the same, too. Only the *generating systems* differ in that each surface rings of PAS1 (starting from the second one) consists of $3n$ C^1-connected bi-3 patches and joins its predecessor C^1.

The contracting rings are shown in Fig. 8a: they have the layout of CC subdivision surfaces, except that the first ring is taken from PAS2 for better transition quality, as demonstrated in Fig. 14. The light-gray underlaid BB-subnet in Fig. 8a C^1-extends the dark-gray BB-net of the first ring of PAS2. Subsequent bi-3 rings are constructed by (b) C^1 extension outwards and (c) splitting of the L-shaped bi-3 tensor-borders $\hat{\mathbf{b}}$ (marked as ○ in Fig. 8b). I.e. $\hat{\mathbf{b}} := \hat{R}\mathbf{d}$, where $\hat{R} := \hat{f}\circ R$ and $\hat{f}$ is defined as follows, see Fig. 6. The 2×2 jets at the corners of the bi-4 tensor-border, see Fig. 6 *right,middle*, are transformed by the map $\hat{f}$ to yield the bi-3 tensor-border displayed in Fig. 6d. Explicitly,

$$\begin{aligned}\hat{\mathbf{b}}_{00} &:= \mathbf{b}_{00},\quad \hat{\mathbf{b}}_{10} := \frac{1}{3}(-\mathbf{b}_{00}+4\mathbf{b}_{10}),\\ \hat{\mathbf{b}}_{11} &:= \frac{1}{9}(\mathbf{b}_{00}-4\mathbf{b}_{10}-4\mathbf{b}_{01}+16\mathbf{b}_{11}).\end{aligned} \tag{5}$$

The remaining BB-coefficients are defined by symmetries: $\hat{\mathbf{b}}_{01}$ is obtained from $\hat{\mathbf{b}}_{10}$ by replacing $\mathbf{b}_{ij}$ by $\mathbf{b}_{ji}$; $\hat{\mathbf{b}}_{2j}$ and $\hat{\mathbf{b}}_{3j}$ $j=0,1$ are obtained from $\hat{\mathbf{b}}_{1,j}$ and $\hat{\mathbf{b}}_{0,j}$ by replacing $\mathbf{b}_{ij}$ by $\mathbf{b}_{4-i,j}$. The sector-diagonal and rotational symmetries then define the required n C^1-connected L-shapes. Splitting $\hat{\mathbf{b}}$ defines the light-gray underlaid BB-sub-net of the new ring, see Fig. 8c. C^1 extension of $\hat{\mathbf{b}}$ outwards defines the dark-gray BB-sub-net of the prior ring, i.e. the prior and the new ring join C^1. Note that only this generating system needs to be defined since the rules $(\mathbf{d},\mathbf{C})\to(\tilde{\mathbf{d}},\mathbf{C})$ are the same for PAS1 as for PAS2. Analogous to PAS2, injectivity of the characteristic ring is checked numerically and by observing that the ring's BB-nets are visually identical to those of Catmull-Clark subdivision.

6. Assessment and Comparison

In all examples, except Fig. 15, and Fig. 16, the input is an extended $\mathbf{c}$-net, i.e. a $\mathbf{c}$-net plus one layer of quads. We choose extended $\mathbf{c}$-nets, because many existing models have been conceived with this structure, and because the extension allows us to generate one surrounding green bi-3 (uniform B-)spline ring for assessing the transition from the regular B-spline surface to the subdivision surface. Larger models are not required, since subdivision is local and interrogation focuses just on a vicinity of n-valent configurations. All figures captioned MM subdivision assume one initial CC refinement step required to join smoothly to the surrounding bi-3 splines, see Fig. 1d,e.

Fig. 9 juxtaposes MM subdivision [MM18] and PAS2. The flaw in the highlight line distribution of Fig. 9c is due to MM subdivision not recovering from artifacts introduced in the CC refinement step needed to transition. Fig. 9d shows that PAS2 fares better even with the handicap of a CC step and Fig. 9e shows that PAS2 by itself yields the most desirable, namely uniform highlight line distribution.

Fig. 10 compares MM to PAS2 and PAS1. MM subdivision yields oscillations in the transition area to the surrounding regular bi-3 surface, while PAS2 and PAS1 have no such shape artifacts and look alike. Fig. 17 zooms in to layers 6,7,8,9 of the subdivision surface, expands the comparison to include degree bi-3 guided curvature bounded subdivisions [KP19], both for a 3×3 macro-patch and a 2×2 macropatch. The 2×2 macro-patch and *PAS2*

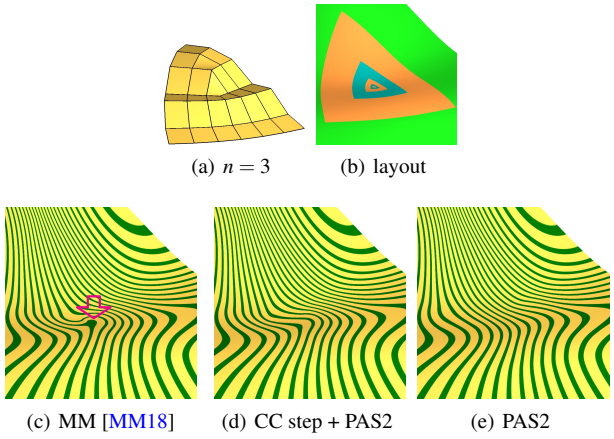

Figure 9: *The case $n = 3$ yields poor highlight lines for MM subdivision.*

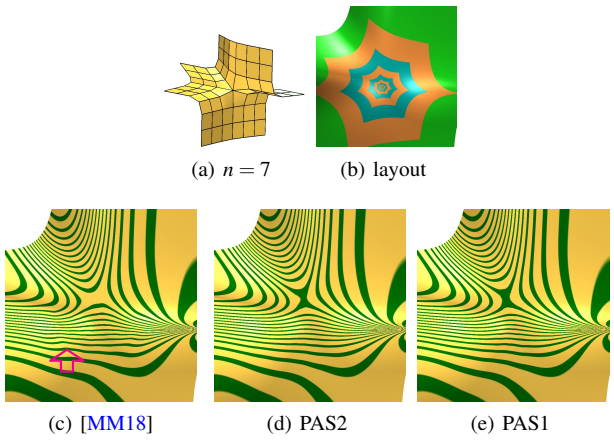

Figure 10: *Saddle input, $n = 7$, yields oscillations for MM subdivision.*

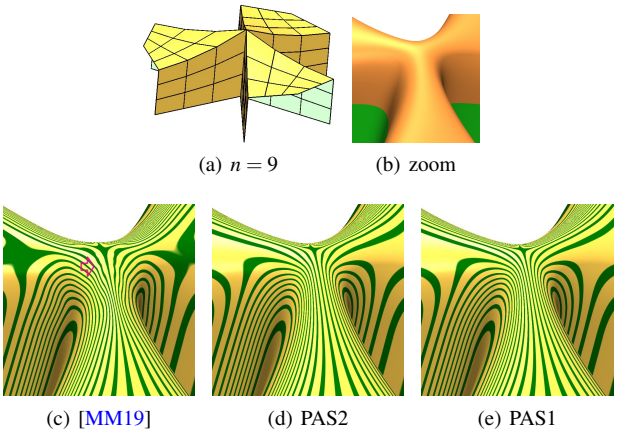

Figure 11: *High valence $n = 9$*

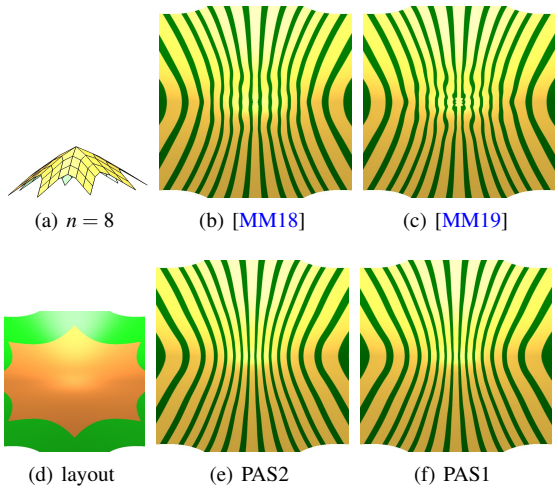

Figure 12: *Convex input, $n = 8$, yields oscillations for MM subdivision.*

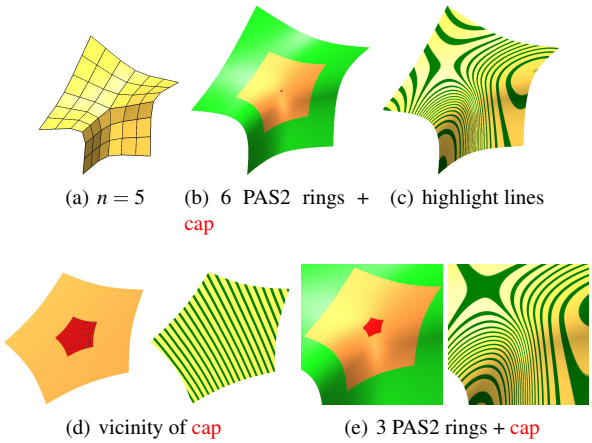

Figure 13: *PAS2 rings completed by a tiny bi-3 cap. (d) vicinity of the cap in (b). (e) Completion after fewer PAS2 rings.*

have the same structure and very similar curvature and highlight line distributions, even though the method in [KP19] requires the separate construction of a guide surface, while *PAS*2 requires only uniformly applied subdivsion rules.

Fig. 11 extends the comparison to [MM19] and confirms robustness of PAS2 and PAS1 also for high valences.

Fig. 12 compares MM to PAS2 and PAS1 for a convex input mesh. Although MM-subdivision improves over earlier conventional subdivision algorithms, the artifacts for convex data, typical for conventional subdivision, still remain. Again PAS2 and PAS1 show no oscillations and look alike.

Fig. 13 shows that PAS2 (or PAS1) generate a high-quality sequences of rings for a finite cap. For example, we can adjust to the **d**-net setting the 2×2 patches per sector construction of [KP15] to serve as a bi-3 cap. Although this cap joins the last subdivision

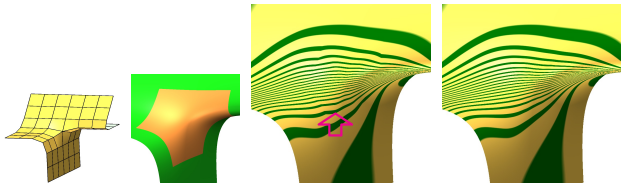

(a) $n = 6$ (b) PAS1 (c) all rings C^1 (d) 1st ring PAS2

Figure 14: *Justification for starting PAS1 with a* 2×2 *ring of PAS2. (b) layout: input ring + subdivision surface.*

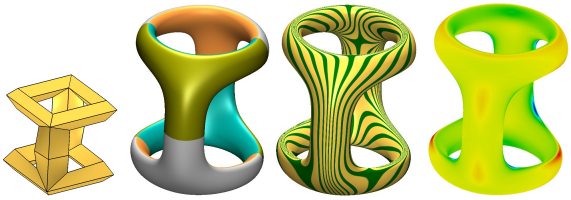

(a) $n = 6$ (b) layout, highlight lines (c) Gauss curvature

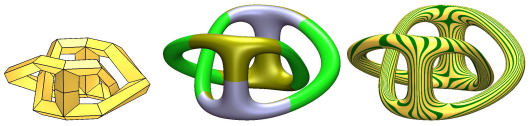

(d) variant I (e) layout, highlight lines

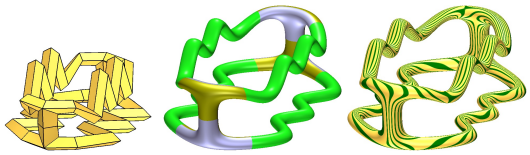

(f) variant II (g) layout, highlight lines

Figure 15: *Quad meshes with* 8 *irregular nodes of valence* 6.

ring formally only C^0, Fig. 13 does not reveal the location of the cap. This is not surprising since the normal discontinuity between the cap and the nth ring is 4^{-n} of the normal discontinuity, deemed acceptable for class A design in [KP15] and so likely also meets the stringent requirements proposed in [SFK22].

Fig. 14 demonstrates the importance of choosing the first ring for PAS1 from PAS2. Note that Fig. 14c does not show a 'first step artifact' in the sense of M. Sabin [Sab02, SB03, ADS11]. Rather the flaw is right at the transition to the first ring.

The mesh in Fig. 15a defines no regular bi-3 patches and consists only of subdivision regions. For example, the surface of genus 3 in Fig. 15b has four 'pants' [Wik22], each consisting of an inner and an outer region. Such pants can be combined to design arbitrarily complex compound surfaces as demonstrated in the *middle* and *bottom* rows. Fig. 18 shows the highlight line distribution of the inner (front) and outer (back) parts of these pants as a close up.

So far, the examples focused on **c**-nets converted to **d**-nets. Fig. 16a displays a (twice) extended **d**-net and uses formula (2)

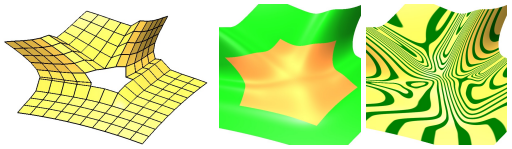

(a) **d**-net, $n = 6$ (b) PAS2 surface

Figure 16: **d***-net,* $n = 6$ *and PAS2 surface with a groove running across the center, and the top region pushed downwards.*

to define **C**. Moreover, a grove and other features have been introduced directly into the **d**-net, making it the primary model representation.

Fig. 19 (and Fig. 17) clearly show the superiority of outcomes for PAS, as well as guided curvature-bounded algorithms [KP19], over the tuned algorithms [MM18, MM19].

7. Conclusion

Despite forty years of progress in the theory and practice of subdivision algorithms [DS78, Sab91, Sta98, HKD93, ZS01, WW01, PR08] and available open source software [Ope22], subdivision surfaces have not been adopted into mainstream engineering design. This is both due to the interpretation as an infinite sequence of polynomial pieces and due to severe shape artifacts. This work addresses the shape artifacts, specifically for the most popular class of surface representations, namely piecewise bi-cubic surfaces. We commented on the second issue by observing that high-quality finite constructions can be obtained by stopping the subdivision algorithm after a few steps and inserting a final cap.

The shape is improved by baking, into the five explicit special PAS subdivision rules, a piecewise polynomial that slightly evolves in each step. This sequence of piecewise polynomials augments and so stabilizes the infinite sequence of surface rings in the sense of empirically preventing visible oscillations. PAS2 subdivision generates a sequence of C^2-joined surface rings and is at least C^1 at the extraordinary point.

For irregular configurations, and higher valence n in particular, C^2 smoothness does not guarantee better highlight lines than C^1. Conversely, naive construction of C^1-joined rings typically results in sharp turns in the highlight lines. It is therefore remarkable that PAS1 can generate frugal C^1 bi-3 surfaces that inherit the good shape of PAS2.

Acknowledgements This work was supported in part by a donation from AMD research.

References

[ADS11] AUGSDÖRFER U. H., DODGSON N. A., SABIN M. A.: Artifact analysis on B-splines, box-splines and other surfaces defined by quadrilateral polyhedra. *Comp Aid Geom Design 28*, 3 (2011), 177–197. 2, 8

[BC94] BEIER K.-P., CHEN Y.: Highlight-line algorithm for realtime surface-quality assessment. *Comp-Aid Design 26*, 4 (1994), 268–277. 1

[CC78] CATMULL E., CLARK J.: Recursively generated B-spline surfaces on arbitrary topological meshes. *Computer-Aided Design 10* (Sept. 1978), 350–355. 1, 2, 3

[dB78] DE BOOR C.: *A Practical Guide to Splines*. Springer, 1978. 2

[dB87] DE BOOR C.: B-form basics. In *Geometric Modeling: Algorithms and New Trends* (1987), Farin G., (Ed.), SIAM, pp. 131–148. 4, 5

[DKT98] DEROSE T., KASS M., TRUONG T.: Subdivision surfaces in character animation. In *Proceedings of the 25th annual conference on Computer graphics and interactive techniques* (1998), pp. 85–94. 2

[DS78] DOO D., SABIN M.: Behaviour of recursive division surfaces near extraordinary points. *Computer-Aided Design 10* (Sept. 1978), 356–360. 2, 8

[Far88] FARIN G.: *Curves and Surfaces for Computer Aided Geometric Design: A Practical Guide*. Academic Press, 1988. 4, 5

[HKD93] HALSTEAD M., KASS M., DEROSE T.: Efficient, fair interpolation using catmull-clark surfaces. In *Proceedings of the 20th annual conference on Computer graphics and interactive techniques, Siggraph 1993* (New York, NY, USA, Aug. 1993), Valastyan L., Walsh L., (Eds.), ACM Press, pp. 35–44. 3, 8

[KP07] KARČIAUSKAS K., PETERS J.: Concentric tesselation maps and curvature continuous guided surfaces. *Computer Aided Geometric Design 24*, 2 (Feb 2007), 99–111. 3

[KP15] KARČIAUSKAS K., PETERS J.: Can bi-cubic surfaces be class A? *Computer Graphics Forum 34*, 5 (August 2015), 229–238. 7, 8

[KP18] KARČIAUSKAS K., PETERS J.: A new class of guided C^2 subdivision surfaces combining good shape with nested refinement. *Computer Graphics Forum 37* (2018), 84–95. 3

[KP19] KARČIAUSKAS K., PETERS J.: Curvature-bounded guided subdivision: biquartics vs bicubics. *Computer Aided Design* (Jul 2019), 1–11. 2, 6, 7, 8, 10

[KP21] KARČIAUSKAS K., PETERS J.: Multi-sided completion of C^2 bi-3 and C^1 bi-2 splines: a unifying approach. *Computer Aided Geometric Design 86* (2021), 101978. PMC - in process. URL: https://www.sciencedirect.com/science/article/pii/S0167839621000236, doi:https://doi.org/10.1016/j.cagd.2021.101978. 2

[KP22] KARČIAUSKAS K., PETERS J.: Bi-cubic scaffold surfaces. *Computer Aided Design 150* (2022), 1–10. 2

[KPR04] KARCIAUSKAS K., PETERS J., REIF U.: Shape characterization of subdivision surfaces – case studies. *Computer-Aided Geometric Design 21*, 6 (july 2004), 601–614. 2

[Lev06] LEVIN A.: Modified subdivision surfaces with continuous curvature. In *ACM SIGGRAPH 2006 Papers*. 2006, pp. 1035–1040. 3

[Ma05] MA W.: Subdivision surfaces for CAD—an overview. *Computer-Aided Design 37*, 7 (2005), 693–709. 2

[MM18] MA Y., MA W.: Subdivision schemes with optimal bounded curvature near extraordinary vertices. *Computer Graphics Forum 37*, 7 (Oct 2018), 455–467. 1, 2, 3, 6, 7, 8, 10

[MM19] MA Y., MA W.: Subdivision schemes for quadrilateral meshes with the least polar artifact in extraordinary regions. *Comput. Graph. Forum 38*, 7 (2019), 127–139. 2, 7, 8, 10

[Ope22] OPENSUBDIV: Opensubdiv, 2022. June 09. URL: https://graphics.pixar.com/opensubdiv/docs/intro.html. 8

[PR08] PETERS J., REIF U.: *Subdivision Surfaces*, vol. 3 of *Geometry and Computing*. Springer-Verlag, New York, 2008. 2, 8

[Pra97] PRAUTZSCH H.: Freeform splines. *Comput. Aided Geom. Des 14*, 3 (1997). 3

[Sab91] SABIN M. A.: Cubic recursive division with bounded curvature. In *Curves and surfaces*. Elsevier, 1991, pp. 411–414. 2, 8

[Sab02] SABIN M.: Subdivision surfaces. In *Handbook of Computer Aided Geometric Design, Ch 12* (2002), Elsevier, pp. 309–341. 8

[SB03] SABIN M., BARTHE L.: Artifacts in recursive subdivision surfaces. In *Curve and Surface Fitting*, Cohen A., Merrien J. L., Schumake L. L., (Eds.). Nashboro Press, http://www.nashboro.com, 2003, pp. 353–362. URL: http://www.irit.fr/~Loic.Barthe/publications.php. 2, 8

[SFK22] SABIN M. A., FELLOWS C., KOSINKA J.: CAD model details via curved knot lines and truncated powers. *Comput. Aided Des. 143* (2022), 103137. 8

[Sta98] STAM J.: Exact evaluation of Catmull-Clark subdivision surfaces at arbitrary parameter values. In *Proceedings of the 25th annual conference on Computer graphics and interactive techniques* (1998), pp. 395–404. 8

[Wik22] WIKIPEDIA CONTRIBUTORS: Pair of pants (mathematics) — Wikipedia, the free encyclopedia, 2022. [Online; accessed 10-June-2022]. URL: https://en.wikipedia.org/w/index.php?title=Pair_of_pants_(mathematics)&oldid=1083381496. 8

[WW01] WARREN J., WEIMER H.: *Subdivision methods for geometric design: A constructive approach*. Elsevier, 2001. 8

[ZS01] ZORIN D., SCHRÖDER P.: A unified framework for primal/dual quadrilateral subdivision schemes. *Computer Aided Geometric Design 18*, 5 (2001), 429–454. 8

Appendix

By symmetry of construction, for $i,j \in \{0,1,2\}$ and noting that the superscript '3' identifies nodes on the sector-separating line:

$$\begin{aligned} a_{ij}^{r,hk} &= a_{ji}^{-r,kh},\ h=1,2,\ k=1,2,\\ a_{3j}^{r,hk} &= a_{3j}^{-r-1,kh},\ h=1,2,\ k=1,2,\\ a_{ij}^{r,3k} &= a_{ji}^{-r+1,3k},\ k=1,2,\\ a_{3j}^{r,3k} &= a_{3j}^{-r,3k},\ k=1,2. \end{aligned}$$

Finally, the weights $a_{ij}^{r,hk}$ can be truncated to 5 digits after the decimal point while still retaining good highlight line distributions. The A_{ij}^{n} entries are therefore shown scaled by 10^5 for easy readability. Note that these are the exact rules used and not their approximation. The tables have negative entries. In our experience negative entries are needed in multi-sided guided constructions to avoid poor highlight lines, e.g. regions that are too flat.

For $n=3$,

$$A_{11}^{3} := \begin{pmatrix} 29 & -324 & -1180 & -408 & -324 & 3673 & 13243 & 4550 & -1180 & 13243 & 38397 & 7783 \\ 0 & -2 & 28 & 179 & -8 & 24 & 4 & -1235 & 29 & -791 & -1743 & -2646 \end{pmatrix}$$

By the symmetries, the third row of the complete matrix A_{11}^{3} is $0,-8,29,-408,-2,24,-791,4550,28,4,-1743,7783$.

$$A_{22}^{3} := \begin{pmatrix} -4 & 28 & -372 & -523 & 28 & -155 & 2704 & 3157 & -372 & 2704 & 12760 & 8911 \\ 2 & -8 & 81 & 504 & -24 & 69 & -21 & -3428 & 141 & -1461 & -3244 & -7471 \end{pmatrix}$$

$$A_{21}^{3} := \begin{pmatrix} 4 & -32 & -899 & -1292 & -27 & 184 & 10310 & 13349 & -405 & 2298 & 24671 & 23239 \\ 0 & 3 & 13 & 212 & -10 & 3 & 257 & -1717 & 42 & -1081 & -1261 & -3102 \\ 1 & -13 & 127 & -244 & -3 & 30 & -945 & 804 & 57 & -42 & -2596 & 5496 \end{pmatrix}$$

$$A_{31}^{3} := \begin{pmatrix} -2 & 8 & -312 & -1547 & 27 & -107 & 3102 & 17560 & -6 & 266 & 4299 & 27262 \\ -2 & 27 & -6 & 320 & 8 & -107 & 266 & -2187 & -312 & 3102 & 4299 & -5305 \\ 2 & -19 & 174 & 320 & -19 & 98 & -830 & -2187 & 174 & -830 & -3461 & -5305 \end{pmatrix}$$

$$A_{32}^{3} := \begin{pmatrix} -1 & 1 & -103 & -510 & 16 & -48 & 509 & 4334 & -21 & 248 & 1294 & 8911 \\ -1 & 16 & -21 & 352 & 1 & -48 & 248 & -2522 & -103 & 509 & 1294 & -5684 \\ 2 & -19 & 172 & 352 & -19 & 101 & -997 & -2522 & 172 & -997 & -3968 & -5684 \end{pmatrix}$$

For $n=5$,

$$A_{11}^{5} := \begin{pmatrix} -169 & -89 & -609 & -547 & -89 & 4446 & 9015 & 5080 & -609 & 9015 & 48998 & 9500 \\ -43 & 102 & -25 & 10 & 56 & -108 & -108 & -47 & 70 & -596 & -636 & -671 \\ 49 & -49 & -77 & 36 & -70 & -125 & 424 & -37 & -43 & 472 & -747 & -989 \end{pmatrix}$$

$$A_{22}^{5} := \begin{pmatrix} -825 & 1369 & 774 & -529 & 1369 & -572 & -6758 & 2039 & 774 & -6758 & 39567 & 15570 \\ -127 & 326 & -116 & 80 & 127 & -292 & -219 & -357 & 142 & -343 & 646 & -4035 \\ 259 & -305 & -334 & 185 & -396 & -374 & 1977 & -268 & -191 & 2213 & -4438 & -5035 \end{pmatrix}$$

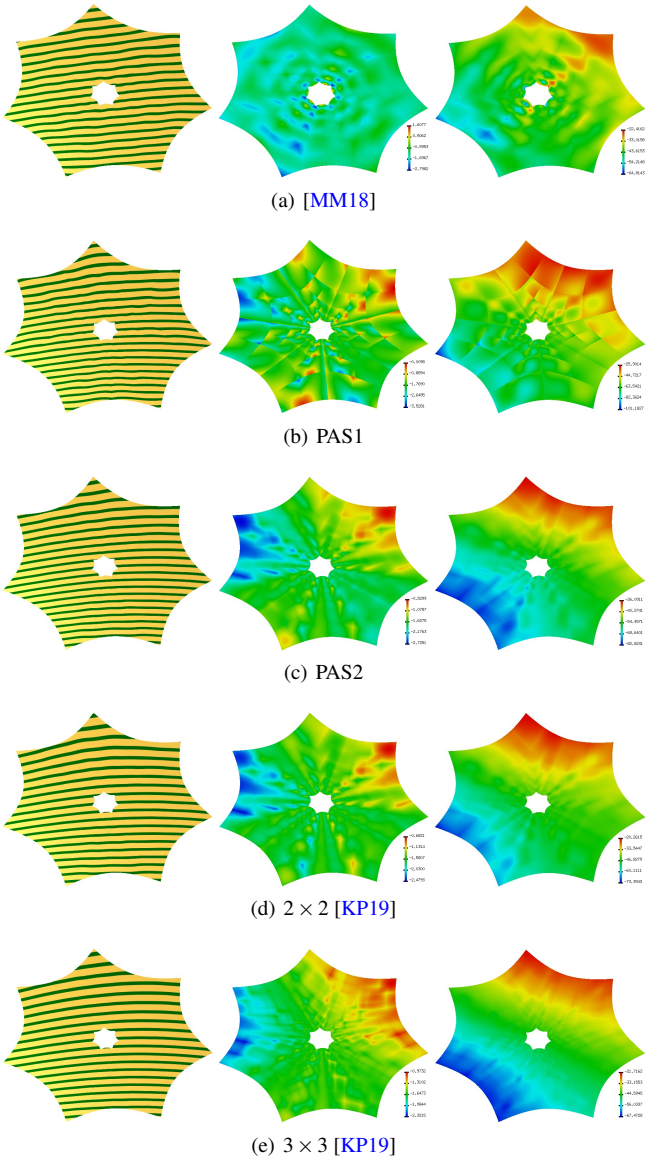

(a) [MM18]

(b) PAS1

(c) PAS2

(d) 2×2 [KP19]

(e) 3×3 [KP19]

Figure 17: *Saddle input $n = 7$ as in Fig. 10. (a) close up of rings 6,7,8,9. Each row shows: highlight line distribution, mean curvature, Gauss curvature.*

$$A^5_{21} := \begin{pmatrix} -436 & 717 & -474 & -1038 & 816 & -577 & 6589 & 10093 & 482 & -3950 & 41098 & 27888 \\ -196 & 382 & -4 & 0 & 283 & -228 & -853 & -104 & 0 & -423 & 1624 & -1061 \\ 139 & -161 & -166 & 84 & -227 & -189 & 1046 & -97 & -59 & 1176 & -2442 & -2251 \\ 94 & -117 & -132 & 63 & -92 & -276 & 949 & -188 & -167 & 836 & -1319 & -2501 \\ 43 & -104 & 90 & -361 & -3 & -154 & 268 & 1532 & -111 & 543 & -1477 & 5189 \end{pmatrix}$$

$$A^5_{31} := \begin{pmatrix} -397 & 610 & 95 & -1630 & 688 & -255 & -468 & 16006 & 4 & -1733 & 12125 & 45503 \\ -397 & 688 & 4 & -14 & 610 & -255 & -1733 & -169 & 95 & -468 & 12125 & 973 \\ 150 & -165 & -182 & 102 & -272 & -167 & 1176 & -203 & 6 & 1153 & -2528 & -3209 \\ 112 & -123 & -191 & 102 & -123 & -332 & 1070 & -203 & -191 & 1070 & -1557 & -3209 \end{pmatrix}$$

$$A^5_{32} := \begin{pmatrix} -659 & 999 & 418 & -562 & 1161 & -422 & -4176 & 2280 & 58 & -3141 & 11858 & 28868 \\ -659 & 1161 & 58 & -62 & 999 & -422 & -3141 & -65 & 418 & -4176 & 11858 & 934 \\ 288 & -340 & -322 & 208 & -531 & -175 & 2140 & -477 & 54 & 1879 & -4901 & -6562 \\ 257 & -329 & -343 & 208 & -329 & -440 & 2161 & -477 & -343 & 2161 & -4207 & -6562 \end{pmatrix}$$

For $n = 6$,

$$A^6_{11} := \begin{pmatrix} 412 & -1269 & 229 & -533 & -1269 & 6942 & 7077 & 4514 & 229 & 7077 & 50796 & 10261 \\ 497 & -528 & 12 & 366 & -870 & 275 & 569 & -1237 & 413 & 163 & -1674 & 593 \\ 293 & -288 & -147 & 162 & -392 & -229 & 972 & -146 & -116 & 1254 & -1301 & -977 \\ -32 & 138 & -225 & 162 & 138 & -469 & 462 & -146 & -225 & 462 & -75 & -977 \end{pmatrix}$$

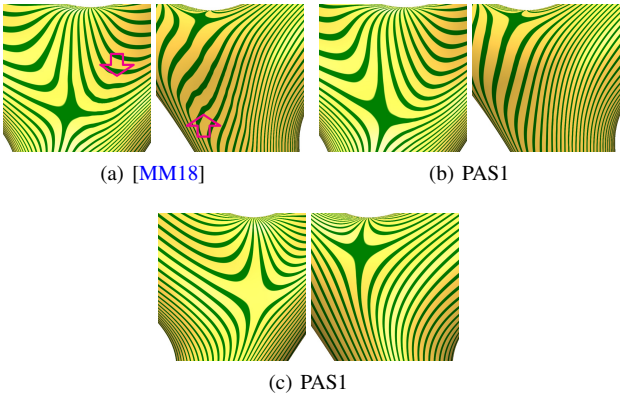

(a) [MM18]

(b) PAS1

(c) PAS1

Figure 18: *Close up of Fig. 15 (left) inner and (right) outer caps of pants, valence $n = 6$. (top) of net Fig. 15a, (bottom) of net Fig. 15d.*

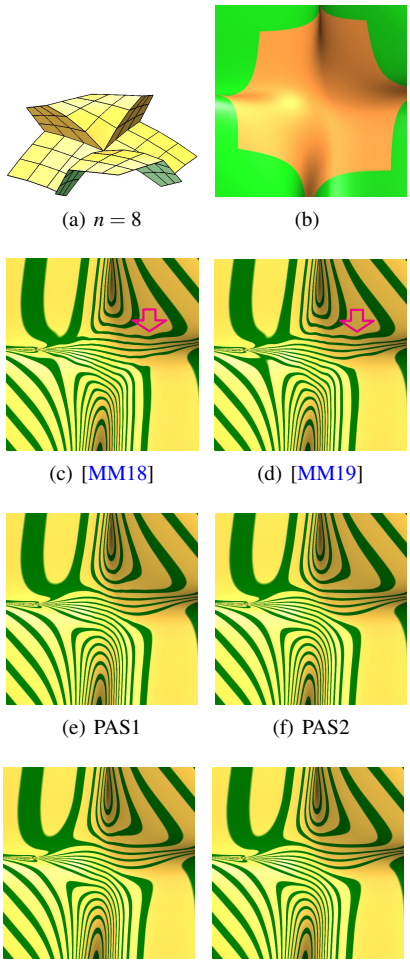

(a) $n = 8$

(b)

(c) [MM18]

(d) [MM19]

(e) PAS1

(f) PAS2

(g) 2×2 [KP19]

(h) 3×3 [KP19]

Figure 19: *Saddle, $n = 8$.*

$$A^6_{22} := \begin{pmatrix} 1114 & -1849 & 2620 & 481 & -1849 & 2484 & -7163 & -4795 & 2620 & -7163 & 40846 & 21191 \\ 1697 & -1683 & -34 & 1196 & -3175 & 1141 & 1743 & -3798 & 1238 & 2927 & -2036 & 402 \\ 824 & -684 & -684 & 292 & -1104 & -1022 & 3446 & 923 & -587 & 4679 & -5799 & -6053 \\ -623 & 1228 & -1023 & 292 & 1228 & -2048 & 1067 & 923 & -1023 & 1067 & -106 & -6053 \end{pmatrix}$$

$$A^6_{21} := \begin{pmatrix} 611 & -1154 & 432 & -311 & -696 & 873 & 7369 & 5445 & 1346 & -4475 & 41503 & 31240 \\ 826 & -838 & 151 & 717 & -1596 & 797 & 109 & -2716 & 548 & 1705 & -468 & 2266 \\ 785 & -806 & -314 & 357 & -1168 & -263 & 2404 & -344 & -91 & 2964 & -3807 & -2617 \\ -208 & 439 & -399 & 95 & 504 & -976 & 500 & 550 & -548 & 791 & 57 & -2263 \\ 220 & -165 & -458 & 623 & -140 & -703 & 1938 & -1650 & -306 & 1295 & -1826 & -1108 \\ 1019 & -1745 & 575 & 66 & -1052 & 316 & 1968 & -1124 & -169 & 1968 & -2924 & 7768 \end{pmatrix}$$

$$A^6_{31} := \begin{pmatrix} 751 & -1485 & 974 & -786 & -870 & 1145 & 1033 & 10362 & 255 & -169 & 9238 & 52321 \\ 751 & -870 & 255 & 848 & -1485 & 1145 & -169 & -3843 & 974 & 1033 & 9238 & 4845 \\ 978 & -991 & -295 & 499 & -1597 & 22 & 2459 & -883 & 187 & 2986 & -3442 & -2545 \\ -83 & 282 & -403 & 28 & 321 & -971 & 844 & 924 & -598 & 1396 & -941 & -2839 \end{pmatrix}$$

$$A^6_{32} := \begin{pmatrix} 1291 & -2680 & 2026 & 921 & -1424 & 2127 & -1588 & -7704 & 627 & -1265 & 7557 & 40263 \\ 1291 & -1424 & 627 & 1308 & -2680 & 2127 & -1265 & -6163 & 2026 & -1588 & 7557 & 8327 \\ 1661 & -1586 & -617 & 768 & -2814 & 27 & 4275 & -883 & 460 & 4981 & -6255 & -6099 \\ -392 & 889 & -897 & -131 & 918 & -1990 & 1422 & 2686 & -1224 & 2493 & -2230 & -7217 \end{pmatrix}$$

For $n = 7$:

$$A^7_{11} := \begin{pmatrix} 2446 & -4043 & 342 & 1295 & -4043 & 8366 & 10056 & -655 & 342 & 10056 & 47956 & 12610 \\ 1709 & -1843 & -289 & 1391 & -2415 & -77 & 3520 & -4022 & 12 & 3646 & -4490 & 2204 \\ 457 & -397 & -237 & 138 & -588 & -372 & 1390 & 133 & -407 & 2078 & -1606 & -1230 \\ -259 & 391 & -73 & -312 & 493 & -464 & -370 & 1398 & -283 & -130 & 620 & -1500 \end{pmatrix}$$

$$A^7_{22} := \begin{pmatrix} 8554 & -10979 & 1580 & 8358 & -10979 & 1418 & 10374 & -27820 & 1580 & 10374 & 26280 & 31517 \\ 5776 & -6099 & -900 & 4147 & -8424 & 8 & 11407 & -11886 & -486 & 15341 & -10823 & 5947 \\ 693 & -227 & -689 & -943 & -1003 & -1191 & 2755 & 4996 & -1378 & 5550 & -4801 & -8009 \\ -2220 & 2978 & -25 & -2775 & 3390 & -1565 & -4401 & 10136 & -877 & -3423 & 4242 & -9105 \end{pmatrix}$$

$$A^7_{21} := \begin{pmatrix} 4219 & -5641 & -343 & 4227 & -5002 & 264 & 16690 & -7759 & 945 & 3582 & 34298 & 37156 \\ 3508 & -3872 & -392 & 2908 & -4976 & 102 & 6689 & -8838 & -559 & 9951 & -7084 & 5946 \\ 1025 & -833 & -525 & 241 & -1518 & -544 & 2901 & 382 & -642 & 4377 & -3641 & -2948 \\ -665 & 878 & -51 & -976 & 1182 & -799 & -994 & 3760 & -644 & -345 & 769 & -3505 \\ -914 & 1416 & -290 & -512 & 1290 & -784 & -1691 & 2488 & -54 & -1938 & 2572 & -3355 \\ 74 & 59 & -785 & 1557 & 72 & -710 & 2002 & -3967 & -240 & 878 & -1668 & 601 \\ 2353 & -3473 & -142 & 3310 & -2350 & -229 & 6199 & -10437 & -586 & 5135 & -5309 & 12009 \end{pmatrix}$$

$$A^7_{31} := \begin{pmatrix} 3816 & -5245 & -2 & 3819 & -4464 & 286 & 9737 & -3278 & -482 & 8142 & 1237 & 60293 \\ 3816 & -4464 & -482 & 3666 & -5245 & 286 & 8142 & -11792 & -2 & 9737 & 1237 & 8762 \\ 1543 & -1402 & -529 & 666 & -2340 & -345 & 3655 & -1068 & -498 & 5304 & -3747 & -1757 \\ -511 & 734 & -101 & -1034 & 888 & -725 & -567 & 4012 & -693 & 350 & -164 & -4071 \\ -1150 & 1643 & -128 & -1034 & 1643 & -755 & -2389 & 4012 & -128 & -2389 & 2974 & -4071 \end{pmatrix}$$

$$A^7_{32} := \begin{pmatrix} 7829 & -10821 & 34 & 10648 & -9107 & 584 & 17036 & -36602 & -718 & 15722 & -9263 & 56449 \\ 7829 & -9107 & -718 & 7095 & -10821 & 584 & 15722 & -22862 & 34 & 17036 & -9263 & 17328 \\ 2908 & -2535 & -978 & 803 & -4552 & -585 & 6670 & -489 & -783 & 9777 & -7021 & -4807 \\ -1664 & 2318 & -129 & -3021 & 2537 & -1445 & -2646 & 11110 & -1348 & -578 & 511 & -10740 \\ -3142 & 4351 & -200 & -3021 & 4351 & -1545 & -6582 & 11110 & -200 & -6582 & 7086 & -10740 \end{pmatrix}$$

For $n = 8$:

$$A^8_{11} := \begin{pmatrix} 4248 & -5998 & -344 & 3385 & -5998 & 7898 & 13951 & -5002 & -344 & 13951 & 45372 & 13702 \\ 2538 & -2543 & -767 & 1958 & -3119 & -1220 & 6102 & -5142 & -841 & 6533 & -6118 & 2764 \\ 23 & 131 & -133 & -370 & -129 & -139 & 229 & 1426 & -459 & 1013 & -271 & -1751 \\ -461 & 502 & 67 & -411 & 707 & -112 & -946 & 1477 & -114 & -891 & 792 & -1269 \\ -67 & 202 & -9 & -411 & 202 & -409 & -248 & 1477 & -9 & -248 & 478 & -1269 \end{pmatrix}$$

$$A^8_{22} := \begin{pmatrix} 14580 & -16481 & -2227 & 16681 & -16481 & -5602 & 28631 & -45696 & -2227 & 28631 & 15433 & 36004 \\ 8498 & -8468 & -2393 & 5766 & -10596 & -3883 & 20050 & -15226 & -3734 & 25186 & -15701 & 8177 \\ -946 & 1610 & 11 & -3167 & 606 & 154 & -2082 & 9982 & -1240 & 925 & 564 & -9155 \\ -3015 & 3301 & 821 & -3655 & 4010 & 366 & -7104 & 11119 & 113 & -6790 & 4912 & -8056 \\ -1712 & 2340 & 555 & -3655 & 2340 & -666 & -4831 & 11119 & 555 & -4831 & 3969 & -8056 \end{pmatrix}$$

$$A^8_{21} := \begin{pmatrix} 6973 & -8077 & -2446 & 8883 & -7497 & -3083 & 25566 & -17711 & -621 & 11713 & 29249 & 39798 \\ 5404 & -5564 & -1509 & 4448 & -6518 & -2522 & 12852 & -12018 & -2635 & 16955 & -11331 & 7277 \\ 375 & -21 & -263 & -907 & -790 & -276 & 971 & 3148 & -874 & 2742 & -1025 & -3561 \\ -1468 & 1599 & 295 & -1486 & 1905 & 256 & -3225 & 4663 & -95 & -2958 & 2161 & -3691 \\ -437 & 583 & 161 & -950 & 810 & -512 & -1242 & 3100 & 96 & -1390 & 1318 & -2204 \\ -808 & 1286 & -9 & -1418 & 862 & -228 & -1982 & 4537 & 234 & -1897 & 1607 & -4105 \\ -973 & 1064 & -437 & 1386 & 1212 & 220 & -1047 & -3326 & 94 & -2025 & 1090 & 889 \\ 2837 & -3714 & -1185 & 6362 & -2643 & -1332 & 8186 & -16761 & -886 & 6726 & -5419 & 13461 \end{pmatrix}$$

$$A^8_{31} := \begin{pmatrix} 5638 & -6605 & -1889 & 7836 & -6022 & -2626 & 16302 & -11885 & -1897 & 14861 & -3090 & 63718 \\ 5638 & -6022 & -1897 & 5694 & -6605 & -2626 & 14861 & -15849 & -1889 & 16302 & -3090 & 9706 \\ 1322 & -1054 & -448 & -81 & -1917 & -631 & 3089 & 709 & -1070 & 5022 & -2151 & -1687 \\ -1360 & 1555 & 284 & -1730 & 1620 & 359 & -3069 & 5283 & -155 & -2465 & 1853 & -4218 \\ -847 & 966 & 295 & -1297 & 1265 & -191 & -2186 & 3982 & 147 & -2283 & 1767 & -2708 \end{pmatrix}$$

$$A^8_{32} := \begin{pmatrix} 12386 & -14544 & -4311 & 20266 & -13173 & -5839 & 33221 & -57632 & -3870 & 31559 & -20071 & 64362 \\ 12386 & -13173 & -3870 & 12088 & -14544 & -5839 & 31559 & -33493 & -4311 & 33221 & -20071 & 20668 \\ 2835 & -2245 & -865 & -578 & -4163 & -1277 & 6436 & 2558 & -2083 & 10196 & -4427 & -4174 \\ -3442 & 3961 & 861 & -4850 & 4010 & 1039 & -8100 & 14447 & -180 & -6558 & 4786 & -11044 \\ -2766 & 3158 & 975 & -4252 & 3755 & 24 & -7190 & 12590 & 616 & -7289 & 5252 & -8463 \end{pmatrix}$$

For $n = 9$:

$$A^9_{11} := \begin{pmatrix} 5133 & -6733 & -1032 & 4731 & -6733 & 7211 & 15893 & -6957 & -1032 & 15893 & 44737 & 13530 \\ 3100 & -2932 & -1282 & 2507 & -3367 & -2443 & 8164 & -6190 & -1605 & 8463 & -7023 & 3321 \\ -153 & 292 & 88 & -998 & 2 & 130 & -473 & 2696 & -414 & 293 & 512 & -1988 \\ -972 & 971 & 309 & -734 & 1093 & 604 & -2445 & 2149 & 263 & -2438 & 1703 & -1612 \\ 146 & -107 & -125 & 232 & 37 & -492 & 450 & -221 & -41 & 281 & -196 & -163 \end{pmatrix}$$

$$A^9_{22} := \begin{pmatrix} 16745 & -17245 & -5418 & 21447 & -17245 & -11656 & 36804 & -52729 & -5418 & 36804 & 13791 & 35207 \\ 10109 & -9570 & -4041 & 7638 & -11054 & -7826 & 26443 & -18996 & -6360 & 30945 & -17903 & 10358 \\ -1147 & 1620 & 750 & -4850 & 597 & 1038 & -3522 & 12670 & -1048 & -786 & 2571 & -8557 \\ -4396 & 4422 & 1732 & -4734 & 4772 & 2990 & -11521 & 12794 & 1463 & -11328 & 7341 & -8462 \\ -1034 & 1191 & 422 & -1828 & 1651 & -400 & -2829 & 5698 & 654 & -3324 & 1576 & -4113 \end{pmatrix}$$

$$A^9_{21} := \begin{pmatrix} 7881 & -8241 & -4092 & 11339 & -7798 & -5870 & 29298 & -21175 & -1953 & 15219 & 28571 & 39376 \\ 6190 & -5972 & -2585 & 5690 & -6603 & -4876 & 16370 & -14185 & -4234 & 20387 & -12742 & 7970 \\ 464 & -174 & -45 & -1570 & -824 & -294 & 956 & 4158 & -1044 & 2511 & -333 & -3014 \\ -2239 & 2275 & 866 & -2460 & 2340 & 1630 & -5849 & 6584 & 623 & -5566 & 3817 & -4395 \\ -578 & 576 & 136 & -225 & 913 & -66 & -1406 & 1107 & 328 & -1796 & 956 & -1047 \\ 346 & -95 & -75 & -1003 & -216 & -911 & 707 & 3008 & -138 & 840 & -576 & -2211 \\ -1478 & 1752 & 552 & -2535 & 1442 & 835 & -3950 & 6666 & 486 & -3732 & 2495 & -4488 \\ -1421 & 1281 & -18 & 1644 & 1575 & 1142 & -2897 & -3993 & 624 & -3844 & 2618 & 1854 \\ 3380 & -3843 & -2012 & 8130 & -3072 & -2593 & 9741 & -19219 & -1283 & 8714 & -5828 & 13052 \end{pmatrix}$$

$$A^9_{31} := \begin{pmatrix} 5935 & -6187 & -3096 & 9406 & -5862 & -4753 & 18196 & -13748 & -2974 & 17377 & -3519 & 63849 \\ 5935 & -5862 & -2974 & 6787 & -6187 & -4753 & 17377 & -17283 & -3096 & 18196 & -3519 & 9453 \\ 1535 & -1283 & -490 & -202 & -1894 & -1125 & 3804 & 623 & -1466 & 5371 & -1895 & -765 \\ -1733 & 1817 & 750 & -2506 & 1709 & 1336 & -4649 & 6564 & 350 & -4093 & 2983 & -4274 \\ -1145 & 1135 & 421 & -1023 & 1400 & 553 & -2966 & 2981 & 514 & -3198 & 1860 & -2062 \\ -20 & 184 & 77 & -1023 & 184 & -515 & -229 & 2981 & 77 & -229 & -28 & -2062 \end{pmatrix}$$

$$A^9_{32} := \begin{pmatrix} 13564 & -14168 & -7380 & 24696 & -13328 & -10950 & 39261 & -63848 & -6472 & 38467 & -22224 & 64978 \\ 13564 & -13328 & -6472 & 15114 & -14168 & -10950 & 38467 & -38201 & -7380 & 39261 & -22224 & 20945 \\ 3588 & -3029 & -1100 & -528 & -4421 & -2586 & 8841 & 1537 & -3103 & 11771 & -4336 & -1716 \\ -4127 & 4345 & 1891 & -6477 & 4044 & 3197 & -11219 & 16849 & 878 & -9797 & 7015 & -10770 \\ -3333 & 3353 & 1385 & -3823 & 3892 & 1834 & -8858 & 10516 & 1497 & -9233 & 5312 & -6828 \\ -1066 & 1453 & 679 & -3823 & 1453 & -367 & -3337 & 10516 & 679 & -3337 & 1476 & -6828 \end{pmatrix}$$